Engineering Fracture Mechanics 274 (2022) 108749

Contents lists available at ScienceDirect

Engineering Fracture Mechanics

journal homepage: www.elsevier.com/locate/engfracmech

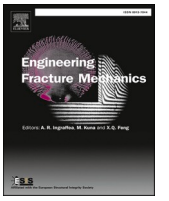

Hydraulic fracture behavior in the presence of hydrogen in notched miniature cylindrical specimens of a 42CrMo4 steel

L.B. Peral [a,b,*], A. Díaz [a], V. Arniella [b], J. Belzunce [b], J. Alegre [a], I.I. Cuesta [a]

[a] University of Burgos, Structural Integrity Research Group, Escuela Politécnica Superior, Avenida Cantabria s/n, 09006 Burgos, Spain
[b] University of Oviedo, SIMUMECAMAT Research Group, Escuela Politécnica Superior de Ingeniería de Gijón, 33203 Gijón, Spain

ARTICLE INFO

Keywords:
Hydrogen embrittlement
Internal high pressure
Hydrogen cathodic precharge
Numerical modelling
HEDE mechanism

ABSTRACT

The influence of internal hydrogen on the mechanical behavior of the 42CrMo4 steel grade has been evaluated by means of internal pressure fracture tests performed on hydrogen precharged notched cylindrical specimens. The notched cylindrical specimens were precharged in a 1 M H_2SO_4 solution + 0.25 g/l As_2O_3 for 3 h and 1.2 mA/cm^2. Thereupon, hydraulic fracture tests were done under different ramps of pressure: 208, 100, 52, 35 and 25 MPa/h, respectively. Hydrogen content introduced into the notched cylindrical specimens (~1 ppm) was determined by thermal desorption analysis (TDA), using a LECO DH 603 hydrogen analyser. Hydrogen damage was observed as testing time increased until 2 h. The burst pressure is reduced around 28 % while the Notch Mouth Opening Displacement decreased around 50 %. Hydrogen embrittlement susceptibility is discussed through the hydrogen embrittlement micromechanisms.

1. Introduction

As the size of a population increases, so does its energy demand. Part of that energy demand is covered through consumption of fossil fuels such as oil, natural gas or coal. However, its intensive use in certain sectors like industry or transport emits significant amounts of greenhouse gases into the atmosphere, such as carbon dioxide or nitrogen oxides. It is important to keep in mind that since 60′s decade, around 350 billion tonnes of carbon have been emitted by humans to the atmosphere [1]. Before climate change becomes irreversible, we must find an alternative fuel that allow us to face the new energy challenges. In this regard, hydrogen emerges as a potential candidate.

In order to cover the increase in energy demand by means of the hydrogen energy, it would be necessary to store and distribute large amounts of hydrogen. Vessels and pipelines have been commonly manufactured from quenched and tempered martensitic steels, belonging to the Cr, Cr-Mo or Cr-Mo-V grades. These types of mechanical components have well shown their ability to deal with hydrogen partial pressures from 3 to 18 MPa [2]. However, the aforementioned increase in energy demand would require attaining higher working pressures, up to 70 or even 100 MPa [3]. Therefore, it is essential to provide a good resistance against the hydrogen embrittlement (HE) phenomenon.

Despite many studies have evaluated the mechanical properties deterioration in martensitic steels in the presence of hydrogen [4–16], there is still no agreement in the scientific community about hydrogen embrittlement mechanisms (HELP & HEDE) and their

* Corresponding author at: University of Burgos, Structural Integrity Research Group, Escuela Politécnica Superior, Avenida Cantabria s/n, 09006 Burgos, Spain.
E-mail addresses: lbperal@ubu.es, luisborja@uniovi.es (L.B. Peral).

https://doi.org/10.1016/j.engfracmech.2022.108749
Received 7 July 2022; Received in revised form 17 August 2022; Accepted 23 August 2022
Available online 27 August 2022

interactions in steels [17,18]. To contribute to this hot point, it is necessary to understand the complex embrittlement phenomenon that takes place when hydrogen diffuses into these metallic components submitted to static and cyclic mechanical loads under hydrogen environments. In order to optimize the performance of the structural steels in hydrogen environments, the complex interaction between hydrogen atoms and the steel microstructure must therefore be taken into consideration. In this respect, hydrogen diffusion and trapping kinetics are controlled by hydrogen trapping sites through the steel microstructure [19,20]. Hydrogen traps can be divided into reversible and irreversible trapping sites depending on the hydrogen binding energy (E_b) [20]. In quenched and tempered martensitic steels, the main hydrogen trapping sites are usually associated to precipitated carbides and ferrite matrix interfaces, martensitic laths, packets and blocks interfaces, grain boundaries and dislocations [21,22].

The definition of the different hydrogen states such as diffusible (interstitial + reversible) and irreversible trapped hydrogen, is necessary to evaluate the impact of hydrogen on the embrittlement mechanisms [23]. In this respect, it is important to highlight that the total hydrogen concentration (interstitial + reversible + irreversible) can be independent of the embrittlement level [24]. In other words, strong trapping sites ($35 \leq E_b \leq 100$ kJ/mol) can contribute to hydrogen remains irreversibly trapped in the steel microstructure. This fact is important to try to increase the yield strength of steels [24], without increasing hydrogen embrittlement susceptibility, by activating HELP and HEDE mechanisms (i.e. irreversible trapped hydrogen does not contribute to the embrittlement process [23,25]). However, although the total hydrogen content is relatively low (~0.5 ppm), hydrogen damage can be noticeable if hydrogen is able to diffuse towards the areas with high stresses level [26,27] by virtue of its diffusion coefficient and the presence of weaker trapping sites (i.e. reversible sites, $10 \leq E_b \leq 30$ kJ/mol) [25]. In this case, when hydrogen diffuses, HELP mechanism promotes that hydrogen is dragged by means of dislocations [18] towards the crack tip region (i.e. embrittlement process area), promoting HEDE mechanisms when a critical hydrogen concentration is reached [28–30]. Definitely, the knowledge of the different hydrogen states and the definition of the trapping site morphology will take an important role on the embrittlement phenomenon, in order to prevent embrittlement micromechanisms [31–33].

Hydraulic fracture tests in the presence of hydrogen are rare in the literature. Therefore, the novelty of this work is focused on the study of the hydrogen embrittlement micromechanisms on hydrogen precharged notched cylindrical specimens submitted to high-pressure hydraulic fracture tests. The decrease in the burst pressure, induced by internal hydrogen effects, has been discussed in terms of the hydrogen embrittlement micromechanims.

2. Material

A low-alloyed ferritic steel from the Cr-Mo family (42CrMo4 grade, AISI4140) has been selected in this study. The chemical composition of the steel, in weight %, is shown in Table 1. The 42CrMo4 steel grade was austenitized at 1200 °C for 20 min, quenched in oil and finally, tempered at 700 °C for 2 h.

The microstructure of the 42CrMo4 steel grade is shown in Fig. 1a. It mainly consists of tempered martensite. A prior austenite grain size (PAGS) of 150 μm was determined. The profuse carbide precipitation (Fe_3C, Fig. 1b) that takes place during the temperature tempering (700 °C and 2 h) can be clearly appreciated in Fig. 1a. Mechanical properties are listed in Table 2, where HV is the Vickers hardness level, σ_{ys} is the yield strength, σ_{uts} is the ultimate tensile strength and A is the elongation at fracture.

3. Experimental procedure

3.1. Hydrogen cathodic precharge

Cylindrical specimens were cathodically precharged with 1.2 mA/cm^2 for 3 h in a 1 M H_2SO_4 + 0.25 g/l AS_2O_3 solution (pH ≈ 1) at room temperature. This current density was enough to ensure that hydrogen available in the solution, H^+, is reduced and partially adsorbed on the steel surface [20]. The experimental set up and the precharged conditions are respectively displayed in Fig. 2.

3.2. Measurement of hydrogen content and desorption at room temperature

In order to know the hydrogen content introduced into the quenched and tempered 42CrMo4 steel grade under the aforementioned conditions (1.2 mA/cm^2 and 3 h), plates with 2 mm thickness were machined (30 × 11 × 2 mm^3). Accordingly, plates were cathodically charged with hydrogen also in a 1 M H_2SO_4 + 0.25 g/l AS_2O_3 solution. Hydrogen content (in wppm) was determined by means of a LECO DH603 hydrogen analyser. The thermal analysis (TDA) to determine hydrogen concentration consists of maintaining the plates at 1100 °C for 300 s.

Hydrogen concentration (C_{H0}) was immediately measured after the hydrogen precharge. Additionally, some of the precharged plates were also exposed to air in different time intervals: 2, 4, 24 h. Finally, they were introduced into the LECO DH603 hydrogen analyser in order to determine the hydrogen desorption curve at room temperature (RT) to estimate the trapping density (N_T) and the

Table 1
Chemical composition of 42CrMo4 steel (weight %).

C	Mn	Si	Cr	Mo
0.42	0.62	0.18	0.98	0.22

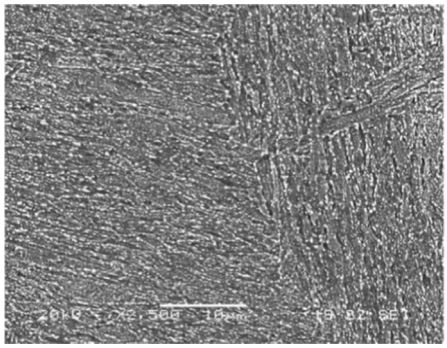

(a)

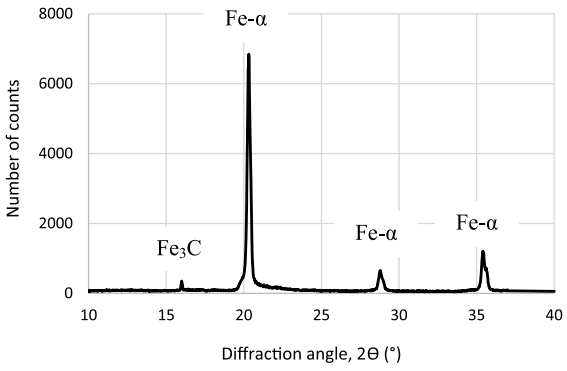

(b)

Fig. 1. (a) SEM microstructure. (b) XRD analysis.

Table 2
Mechanical properties. 42CrMo4 steel grade.

HV_{30}	σ_{ys} (MPa)	σ_{uts} (MPa)	A (%)
230	600	750	24

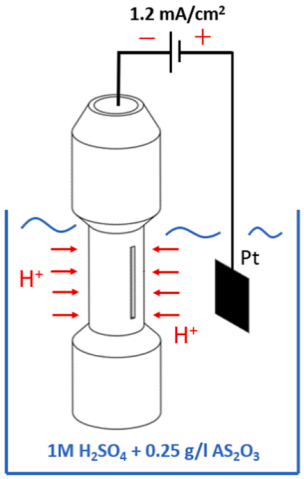

(a)

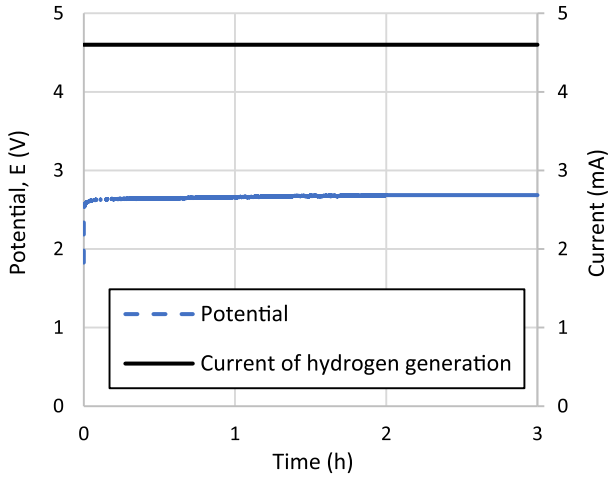

(b)

Fig. 2. (a) Hydrogen precharge (Counter electrode: Platinum, Pt). (b) Galvanostatic charge with 1.2 mA/cm^2. The exposed area into the solution was 3.7 cm^2 → 4.6 mA.

apparent hydrogen diffusion coefficient (D_{app}).

3.3. Hydraulic fracture tests

Hydraulic fracture tests have been conducted in a high-pressure test device that has been manufactured by the research group. It is able to attain 6000 bar of internal pressure. The notched cylindrical specimens were previously precharged with hydrogen (Fig. 2) and then, by means of a piston that is controlled by a MTS820 machine (Fig. 3), water was injected at high pressure until attaining the burst pressure. Pressure ramps of 208, 100, 52, 35 and 25 MPa/h were respectively employed in the different trials in order to analyse the effect of hydrogen accumulation on the notch tip region. It is important to mention that test device is initially filled with water before applying the mentioned ramps of pressure. Then, the miniature specimens were located in the machine and thereupon, high internal pressure was automatically applied, driving the fluid by means of the piston, towards the interior of the notched miniature cylindrical specimens.

The geometry of the notched cylindrical specimens is shown in Fig. 4a. A longitudinal notch of 250 μm depth, 60° angle and tip radius less than 0.1 mm was machined. The ideal ligament length is approximately 250 μm. A detail of the notch geometry is also given in Fig. 4b.

After testing, the burst pressure was corrected by equation (1), where P_b is the corrected burst pressure, P_b' is the experimental burst pressure at the moment of failure and K_{ideal} (equation (2)) and K_{real} (equation (3)) represent the correction factors. $\varnothing_i$ is the internal diameter of the notched miniature cylindrical specimen and b is the final ligament length (equation (3)), which was measured by means of the scanning electron microscope (SEM) after testing each notched miniature specimen. The ideal ligament length is 0.25 mm, equation (2).

$$Pb = Pb' \frac{K_{ideal}^2}{K_{real}^2} \tag{1}$$

$$Kideal = \frac{\varnothing_i + 2 \cdot 0.25}{\varnothing_i} \tag{2}$$

$$Kreal = \frac{\varnothing_i + 2 \cdot b}{\varnothing_i} \tag{3}$$

3.4. SEM and X-Ray diffraction analysis

The microstructure and the fracture surfaces were observed in a scanning electron microscope, JEOL JSM-6460LV. Regarding the microstructural observations, the specimen was ground up to 1200 SiC paper, and then it was polished with 6 and 1 μm diamond paste, respectively. Finally, specimen was etched with Nital-2 %. Additionally, X-ray diffraction analysis was carried out on the surface of the 42CrMo4 steel specimen by means of a Seifert XRD 3000 TT diffractometer (Seifert, Massillon, OH, USA). Patterns were registered by a scintillation detector (Nal (Tl)) between 10° y 40° in 2 Theta on fixed mode. The radiation is emitted by a thin line molybdenum focus working at 40 kV × 40 mA, and it is then monochromatized to the Kα doublet ($\lambda 1 = 0.7093$ Å and $\lambda 2 = 0.7136$ Å) by means of a primary filter of zirconium and a secondary monochromator of highly oriented pyrolytic graphite (HOPG).

3.5. Numerical modelling of stress concentration

Stress-driven hydrogen accumulation around the notch is expected to play a crucial role in the embrittlement process. Therefore, the hydrostatic stress distribution is numerically determined using a 2D plane strain FE model with quadrilateral second-order elements and reduced integration. Only a half of the cross section is simulated because of symmetry, and the corresponding boundary

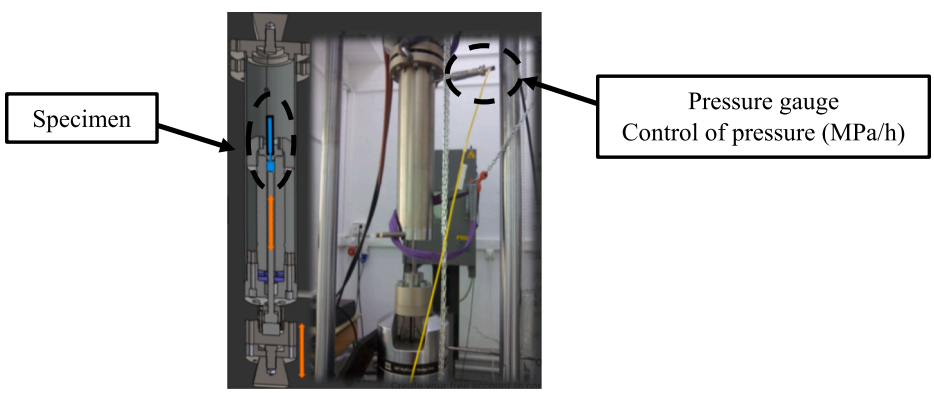

Fig. 3. Experimental set-up.

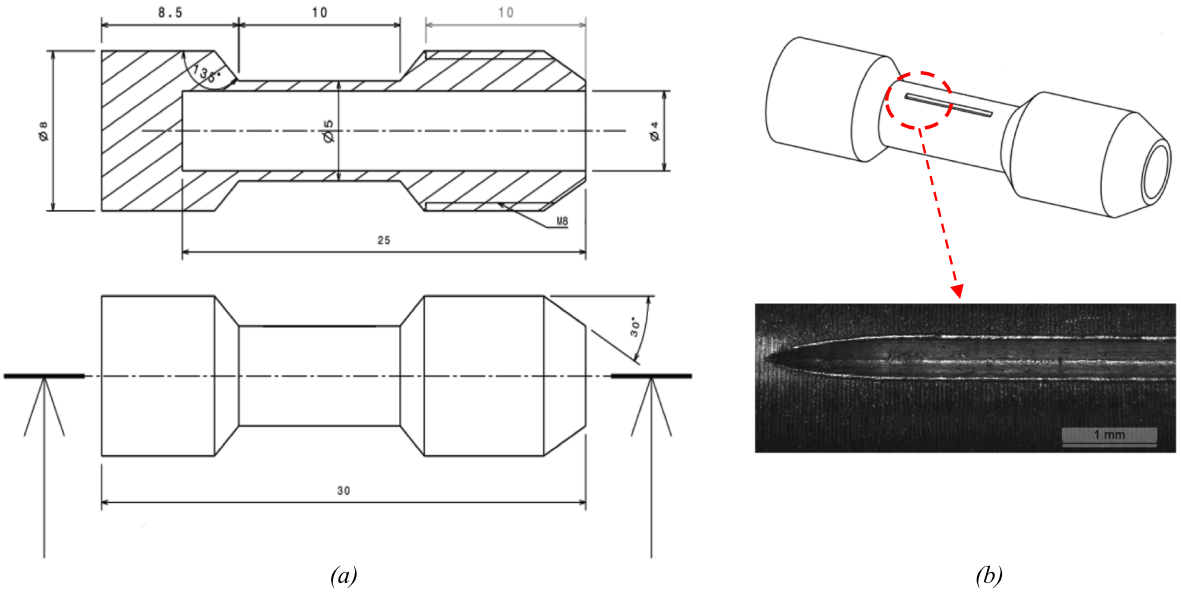

Fig. 4. (a) Notched cylindrical specimen (dimensions in mm). (b) Notch detail.

conditions are imposed. Loading is modelled through a pressure on the inner surface, and the considered material behaviour follows a power-law hardening with the yield stress from Table 2 and a hardening exponent of 0.12 [34]. Young's modulus is taken as E = 210 GPa and the Poisson's coefficient $\nu = 0.3$.

3.6. Numerical modelling of hydrogen desorption

With the aim of assessing the loading rate effect on embrittlement, diffusivity and trapping features are fitted from the experimental desorption curve at room temperature, considering two different numerical modelling approaches. Both of them are implemented in the *transport of diluted species* module in the Finite Element software Comsol Multiphysics.

The simulated geometry is a 3D model of the steel plate of $30 \times 11 \times 2$ mm^3; mesh consists of hexahedral linear elements including 20 elements in the thickness direction, i.e. the direction that controls diffusion during desorption, with a biased distribution in order to obtain a finer mesh near the surface where the concentration gradients are higher.

3.6.1. Apparent diffusivity modelling

A constant and apparent diffusivity D_{app} can be assumed, and the mass diffusion equation is simplified as follows:

$$\frac{\partial C}{\partial t} = D_{app}\nabla^2 C \tag{4}$$

where C is the total hydrogen concentration at each specimen point. In this approach, hydrogen content measured just after precharging represents the initial condition, whereas trapped hydrogen that remains after 24 h is fixed as the boundary condition for the exit surface following the approach from [35].

$$C(\mathbf{x}, t = 0) = C_{H0} = 0.93 \text{ wt ppm} \tag{5}$$

$$C(\mathbf{x} \in \mathscr{S}, t) = C_{H,24} = 0.17 \text{ wt ppm} \tag{6}$$

where $\mathbf{x}$ represents the point coordinates and $\mathscr{S}$ the sample boundary. Fixing initial and boundary conditions from experimental results, D_{app} is obtained by iterating over different values and choosing the curve that minimises the sum of square residuals R at 2 and 4 h.

$$R = \sum_{t=2,4} \left(\overline{C}_t - C_{H,t}\right)^2 \tag{7}$$

$\overline{C}_t$ is obtained by integration over the 3D specimen at time t and $C_{H,t}$ is the corresponding experimental value measured after room temperature desorption.

However, D_{app} does not depend on local concentration in contrast to experimental observations and theoretical demonstrations. A more sophisticated trapping model is required to capture different diffusion regimes depending on the concentration range.

3.6.2. Two-level modelling

Total concentration C can be divided into two species: hydrogen in lattice sites, C_L, and hydrogen in traps, C_T. This two-level strategy has been adopted by many authors for the study of trapping kinetics and hydrogen transport phenomena near a crack tip [36]. Hydrogen flux is here only determined by lattice diffusion, where D_L is the ideal diffusion coefficient:

$$\frac{\partial C_L}{\partial t}+\frac{\partial C_T}{\partial t}=D_L\nabla^2 C_L \tag{8}$$

Assuming thermodynamic equilibrium, the trapping rate can be expressed in terms of C_L and two trap parameters: the binding energy of defects, E_b, and the density of trapping sites, N_T. Applying the chain rule and operating as in [37]:

$$\frac{\partial C_L}{\partial t}=D_L\nabla^2 C_L-\frac{\frac{K_T N_T}{N_L}}{\left[1+\frac{C_L}{N_L}(K_T-1)\right]^2}\frac{\partial C_L}{\partial t} \tag{9}$$

where $K_T=\exp(E_b/RT)$, being R the constant of gases and T the temperature. N_L and N_T represent density of lattice and trapping sites, respectively. Trapping rate is simulated in Comsol Multiphysics including the last term of equation (9) as a reaction term. A zero-concentration boundary condition is now applied to C_L to model instantaneous exit, whereas the initial condition is fixed as $C_L(\mathbf{x},t=0)=\widehat{C}_0-C_{T,0}$, where $C_{T,0}$ is found assuming thermodynamic equilibrium in this approach, D_L must be assumed from theoretical or experimental data. Here, $D_L=6\times10^{-10}$ m^2/s is used following the value obtained by Peral et al. [20]. The residual now is calculated also including the experimental value at 24 h, since the boundary condition is not dependent on that value.

$$R=\sum_{t=2,4,24}\left(\overline{C}_t-C_{H,t}\right)^2 \tag{10}$$

4. Results and discussion

4.1. Measurement of hydrogen content and desorption at room temperature

After hydrogen pre-charging (1.2 mA/cm^2 for 3 h), an initial hydrogen content (C_{H0}) of 0.93 ppm was measured (Fig. 5) by means of the LECO DH603 hydrogen analyser. The residual hydrogen content (strongly trapped) in the steel microstructure was around 0.2 ppm (C_{Hf}). The diffusible hydrogen, that is able to get out from traps and diffuse out of the steel, is approximately 0.73 ppm (C_{H0}-C_{Hf}). This hydrogen amount is associated to hydrogen diffusion from the lattice and reversible trapping sites. At this respect, A. Zafra at el. [38] studied the effect of hydrogen diffusion and trapping in a quenched and tempered 42CrMo4 steel. They reported binding energies (E_b) of 11.8, 17 and 27.4 kJ/mol. These binding energies were respectively associated with reversibly trapped hydrogen between the interfaces Fe_3C precipitated carbides (Fig. 1) and the ferritic matrix (11.8 kJ/mol), hydrogen trapped in lath, block and packet martensite interphases (17 kJ/mol) and the elastic field of dislocations (27.4 kJ/mol). As shown below, these microstructural singularities play an important role on the hydrogen embrittlement process.

Fig. 6 gives the hydrogen trapping and diffusivity parameters that have been obtained after numerical fitting of the experimental desorption curve by minimising square residuals. The apparent diffusion coefficient (D_{app}) has been found to be $7\cdot10^{-11}$ m^2/s (Fig. 6a and b) while a trapping density in the order of $2\cdot10^{24}$ sites/m^3 (equation 11) and binding energy of 47.5 kJ/mol are fitted from the two-level approach in this microstructure. This binding energy is related to trapped hydrogen in the core of the dislocation [20] and also would contribute to justify the residual hydrogen content that is irreversibly trapped in the steel microstructure (~0.2 ppm, Fig. 5a).

$N_T=n\cdot N_L$ (11).

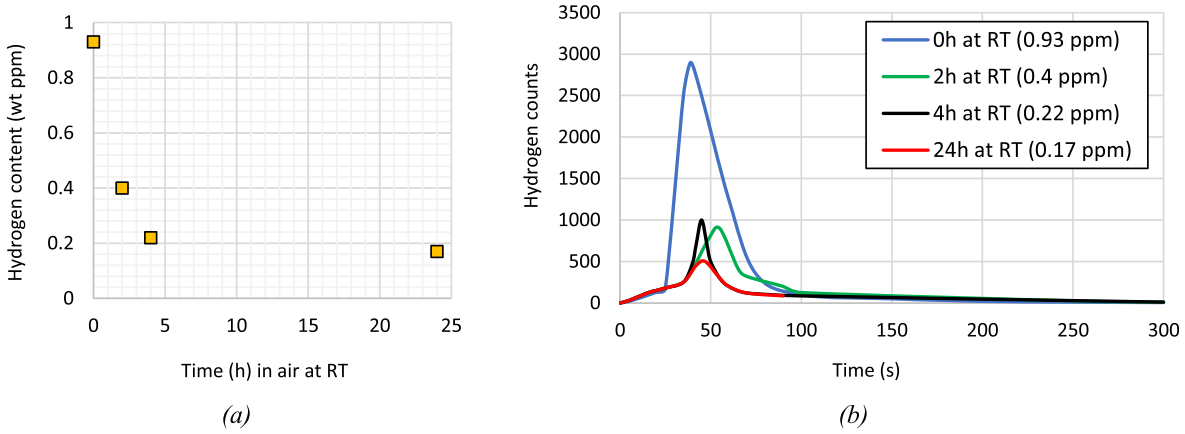

Fig. 5. (a) Experimental hydrogen desorption curve at room temperature. *(b) Thermal desorption profiles at 1100 °C for 300 s in the hydrogen analyser LECO DH603.*

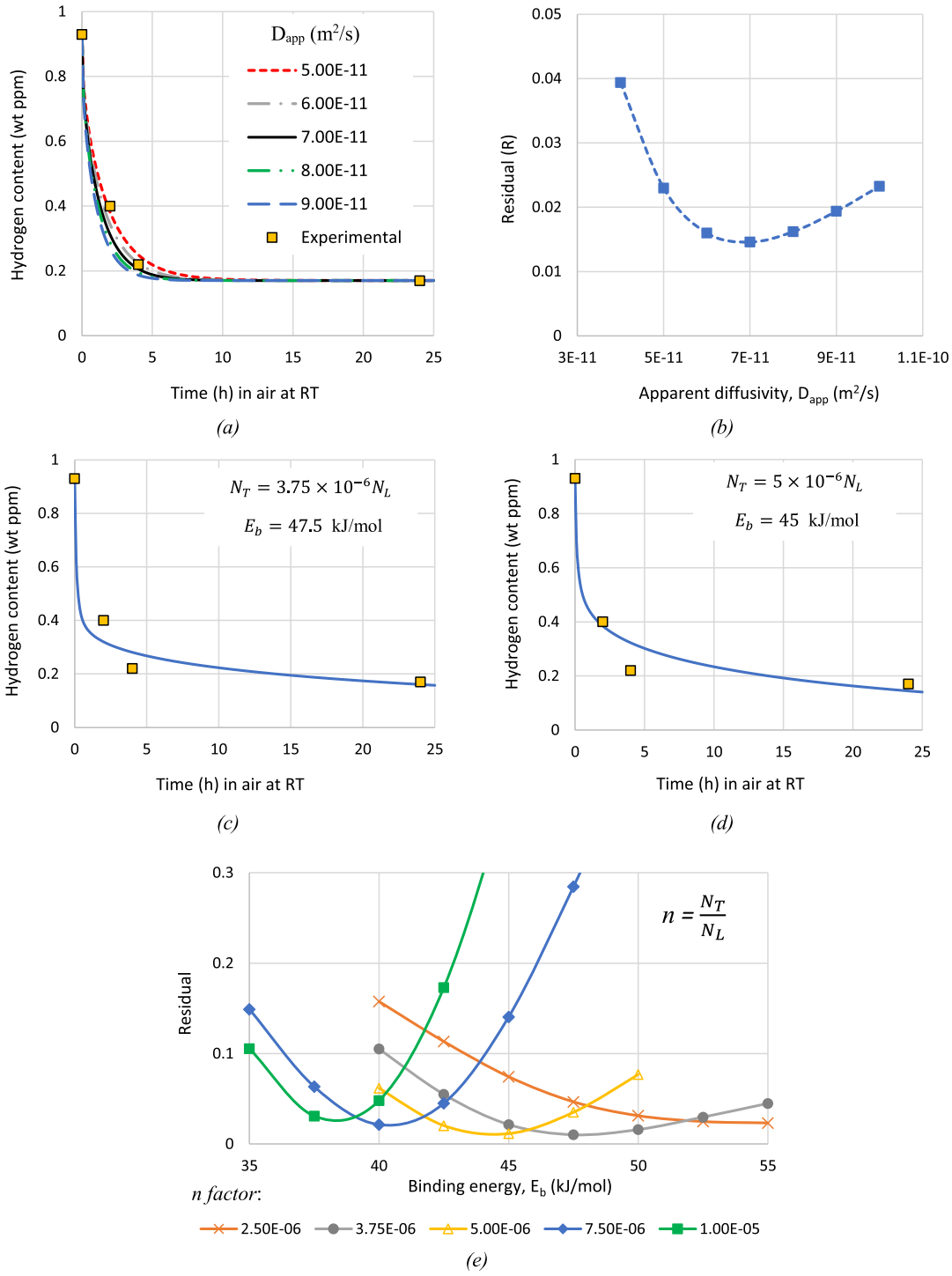

Fig. 6. (a, b) Apparent diffusivity modelling. (c, d, e) Two-level modelling approach.

The best data fitting is given by n = $3.75{\cdot}10^{-6}$ (Fig. 6c and e). N_L is considered as $5.1{\cdot}10^{29}$ sites/m^3 for tetrahedral interstitial sites in ferrite lattice [20]. Therefore, the trapping density (N_T) was calculated.

4.2. Hydraulic fracture tests

Fig. 7 gives the variation of the pressure as a function of the time for the uncharged and hydrogen precharged notched cylindrical

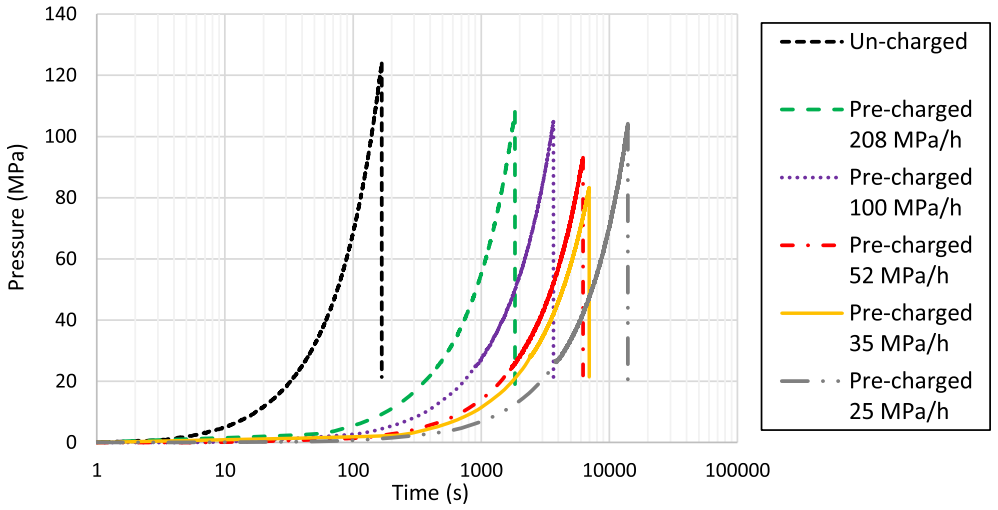

Fig. 7. Hydraulic fracture test curves. Pressure vs. time.

specimens. The latter were tested at different ramps of pressure. Table 3 summarizes the data obtained from the experimental results. P_b is the burst pressure (equation (1)) and the NMOD parameter is the notch mouth opening displacement (Fig. 9). Table 4 shows the embrittlement indexes (EI) related to the burst pressure (P_b) and the NMOD parameter. On the same table, hydrogen embrittlement micromechanisms are also given by order of importance. Hydrogen embrittlement micromechanisms evidenced at 52, 35 and 25 MPa/h are subsequently discussed in the hydrogen fracture micromechanisms section.

Fig. 8 and Fig. 9 show, respectively, the evolution of the burst pressure (P_b) and the notch mouth opening displacement (NMOD) as a function of the applied pressure ramp. The effect of the internal hydrogen was especially noted as the pressure ramp decreases (i.e. as testing time increases), being this effect more pronounced on the NMOD parameter. However, internal hydrogen effect notably diminished for the lowest ramp of pressure (25 MPa/h), presumably, due to the hydrogen fugacity (at RT) for test times greater than 2 h. Besides, after four hours testing, hydrogen atoms (~0.2 ppm, Fig. 5a) remain already strongly trapped into the steel microstructure and the local hydrogen concentration attained in the notch tip region would be lower.

4.3. Hydrogen fracture micromechanisms

Fig. 11 and Fig. 12 give the embrittlement indexes related to the burst pressure (P_b) and the NMOD parameter as a function of the ramp of pressure and the test time, respectively. Hydrogen effect was especially appreciated as the ramp of pressure decreases (Fig. 11), in other words, as hydrogen atoms have more time to diffuse (Fig. 12) towards the notch tip region by virtue of its apparent hydrogen diffusion coefficient ($\sim 7 \cdot 10^{-11}$ m^2/s, Fig. 6a and b).

When a tensile load is applied on a notched specimen, diffusible hydrogen (lattice and reversible) located in the surroundings of the notch will diffuse towards the notch-tip area motivated by the high hydrostatic stress existing in this region (Fig. 10 and Fig. 17). In this situation, when a critical hydrogen concentration is reached, the hydrogen embrittlement mechanisms (HELP & HEDE) can take place, contributing to decrease the burst pressure of the notched miniature cylindrical specimens and especially, to reduce the notch mouth opening displacement (NMOD).

Fig. 13 shows the general fracture surfaces corresponding to the specimens tested under the different ramps of pressure. From a visual point of view, it is important to appreciate that the notch mouth opening displacement (NMOD) was notably lower on the hydrogen precharged specimens, tested at 52 (d) and 35 MPa/h (e), respectively.

Fig. 14 displays the fracture surface corresponding to the un-charged specimen (P_b = 115 MPa and NMOD = 1.98 mm), which showed a ductile micromechanism, consisting of initiation, growth and coalescence of microvoids, MVC.

Fig. 15 gives the fracture surfaces of the hydrogen precharged specimen and tested at 52 MPa/h. These images were taken from the

Table 3
Hydraulic fracture tests results for the different ramps of pressure.

	V_{test} (MPa/h)	Test duration (s)	P_b (MPa)	NMOD(mm)
Uncharged	7000	167	115 ± 10	1.98
H-precharged	208	1842	108	1.67
	100	3690	99	1.51
	52	5752	91 ±3	1.33 ± 0,16
	35	6994	83	1.00
	25	15,000	100 ± 5	1.66

Table 4
Embrittlement indexes (EI) and fracture micromechanisms by order of importance. *MVC: microvoids coalescence, MLD: martensitic lath decohesion, CMD: carbides matrix decohesion, QC: quasi-cleavage. EI (%) $=\frac{X_{no-H}-X_H}{X_{no-H}}\cdot 100$.

	V_{test} (MPa/h)	EI P_b (%)	EI NMOD (%)	*Fracture micromechanism
Uncharged	7000	–	–	MVC
H-precharged	208	6	16	MVC
	100	14	24	MVC + CMD + MLD (observed very locally)
	52	20 ± 3	33	MVC + MLD (60 μm) + CMD
	35	28	50	MVC + MLD (80 μm) + CMD/QC + microcracks
	25	13 ± 4	16	MVC + CMD

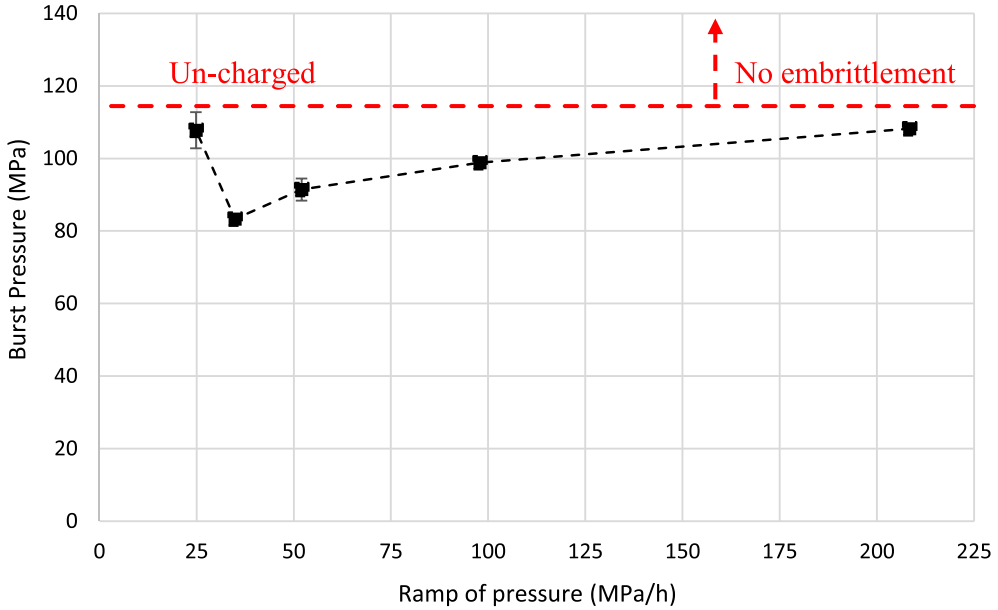

Fig. 8. Burst pressure trend.

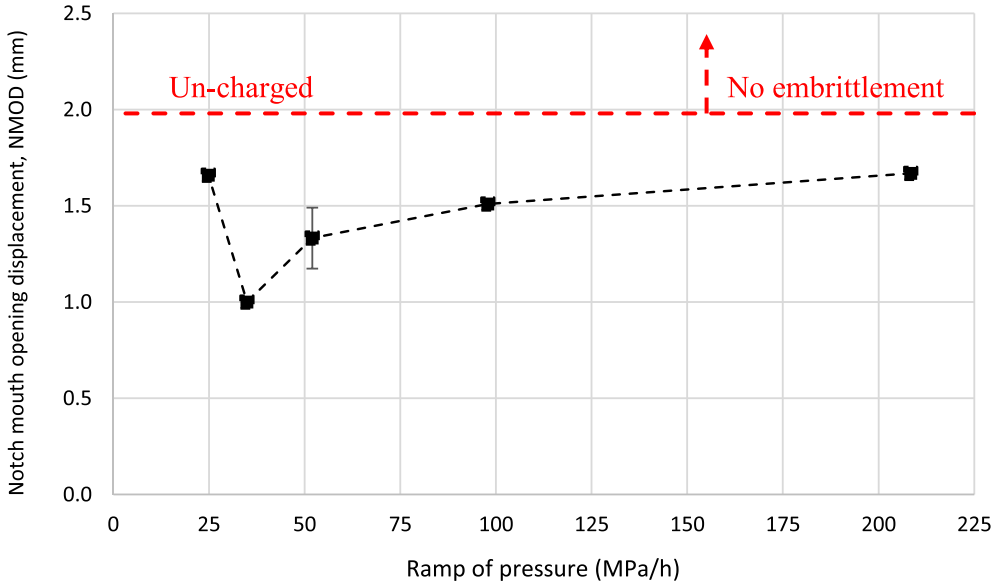

Fig. 9. Notch mouth opening displacement (NMOD) trend.

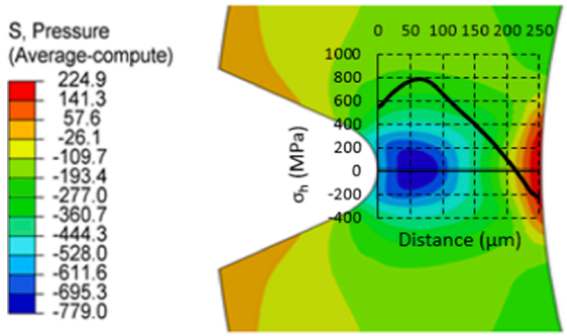

Fig. 10. Hydrostatic stress distribution (MPa) when the applied stress is equal to the burst pressure (91 MPa) at 52 MPa/h.

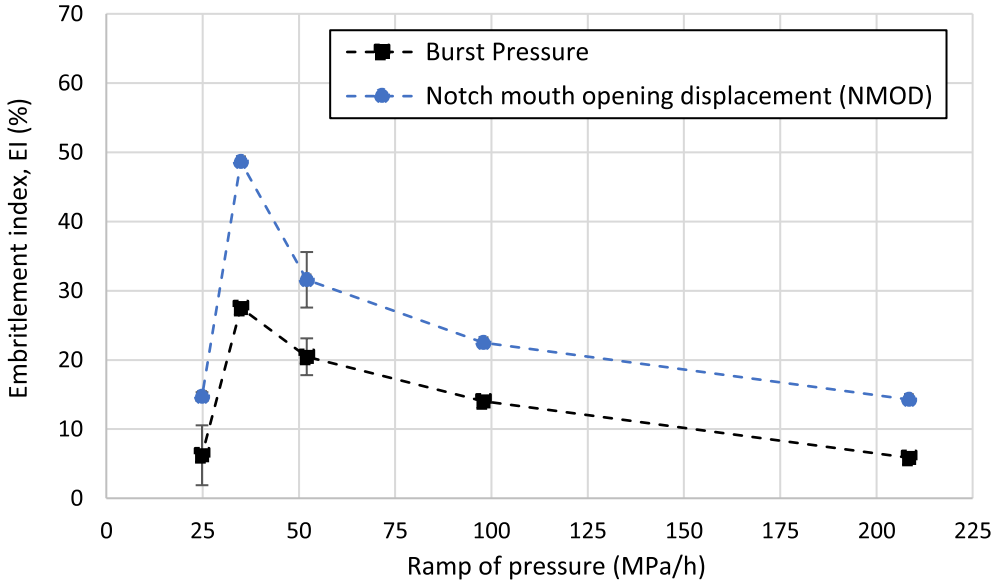

Fig. 11. Embrittlement indexes trend as a function of the applied pressure.

general fracture surface given previously in Fig. 13d.

The main failure micromechanism was ductile (MVC). Nevertheless, the region just ahead the notch tip (first 60 μm, see Fig. 15b), where the hydrostatic stress attains the maximum value ($\sigma_H \sim 779$ MPa, Fig. 10), has the appearance of a transgranular fracture or quasi-cleavage micromechanism (based on HEDE mechanisms, hydrogen enhanced decohesion) that is usually known as PRHIC (plasticity related hydrogen induced cracking) in quenched and tempered steels [39]. It is described as a fracture surface characterized by ductile micro-plastic tearing on a very fine scale, along the martensitic lath interfaces (weak trapping sites, $E_b \sim 17$ kJ/mol). Hence, critical hydrogen concentration reached in these singularities promotes its decohesion in the region near the notch tip (Fig. 15b). This micromechanism is also known as MLD, martensitic lath decohesion. The extension of the region submitted to high hydrostatic stress (60–70 μm in Fig. 10) at the moment of failure matches quite well with the depth of the observed peripheral belt in Fig. 15b. Failure initiates just ahead of the notch under the HEDE mechanism (characterized by the MLD micromechanism) and MVC takes place afterwards along the ligament (Fig. 15d). Additionally, a transition region (Fig. 15c), with very small microvoids, was locally identified after the aforementioned peripheral belt. These microvoids are caused by the decohesion along carbide-matrix interfaces (CMD) motivated by the high local hydrogen concentration attained in these singularities [38], which also act as weak or reversible trapping sites ($E_b \sim 11.8$ kJ/mol). A profuse carbide precipitation had taken place during the tempering treatment (Fig. 1).

On the other hand, Fig. 16 displays now the fracture surfaces of the hydrogen precharged specimen and tested at 35 MPa/h, where hydrogen damage was maximum (see Fig. 11 and Fig. 12). Although the main failure micromechanism was also ductile (MVC, in the bulk of the specimen), a region near the notch tip characterized by martensitic lath decohesion (MLD) and secondary cracks was identified. This region attained a maximum depth of 80 μm corresponding to the high hydrostatic stress area. The adjacent area to this region is shown in Fig. 16b, and it has the appearance of a quasi-cleavage (QC) partially mixed with very small dimples (CMD micromechanism).

Definitely, dislocation movement induces hydrogen accumulation near the notch tip area because of the hydrogen enhanced

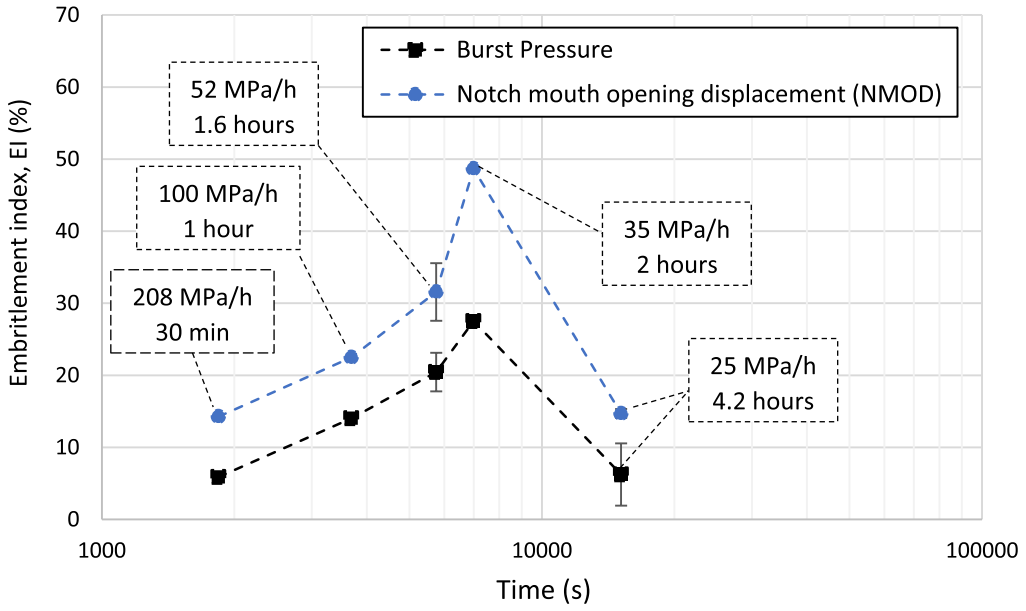

Fig. 12. Embrittlement indexes trend as a function of the testing time. Ramp of pressure and the test time are indicated within the bullets.

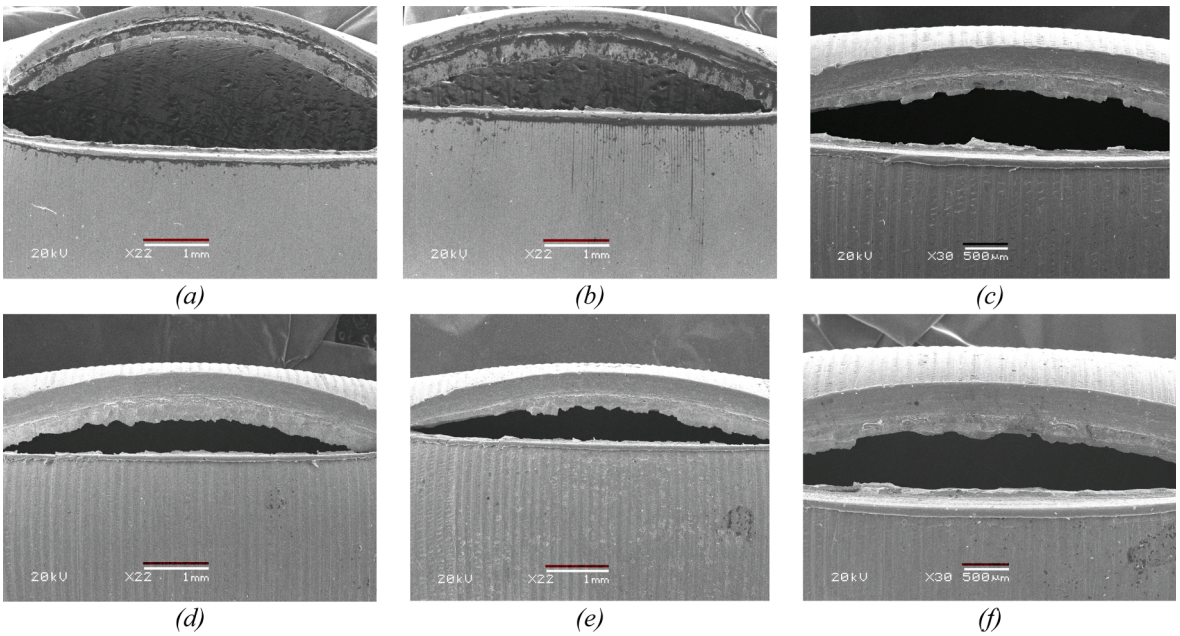

Fig. 13. General fracture surfaces. (a) Un-charged specimen, (b) H-precharged specimen, tested at 208 MPa/h, (c) H-precharged specimen, tested at 100 MPa/h, (d) H-precharged specimen, tested at 52 MPa/h, (e) H-precharged specimen, tested at 35 MPa/h and (f) H-precharged specimen, tested at 25 MPa/h.

localized plasticity (HELP). Therefore, dislocation movement promotes that a critical hydrogen concentration is reached in the notched area (Fig. 17), mainly under 35 and 52 MPa/h. Consequently, HELP mechanism mediated HEDE leads to the fracture along the martensitic lath interfaces (MLD) and decohesion along the carbide-matrix interfaces (CMD). These microstructural locations are also characterized as weak trapping sites for hydrogen atoms.

On the other hand, for the longest test time, 4 h testing or 25 MPa/h, hydrogen damage is partially relieved (Fig. 11 and Fig. 12). Based on Fig. 5, after 3 or 4 h testing, most diffusible hydrogen has already diffused out of the specimens. After this testing time, diffusible hydrogen content reached in the notch area is barely able to trigger the damage mechanisms (HEDE and HELP). In this situation, the failure micromechanism was mainly ductile (Fig. 18). MLD (based on HEDE) or secondary cracks were not observed near

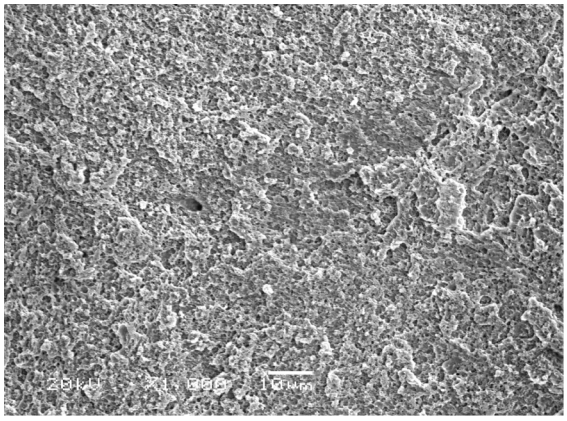

Fig. 14. Un-charged specimen with P_b = 115 MPa and the NMOD = 1,98 mm. Coalescence of microvoids (MVC) detail from Fig. 13a.

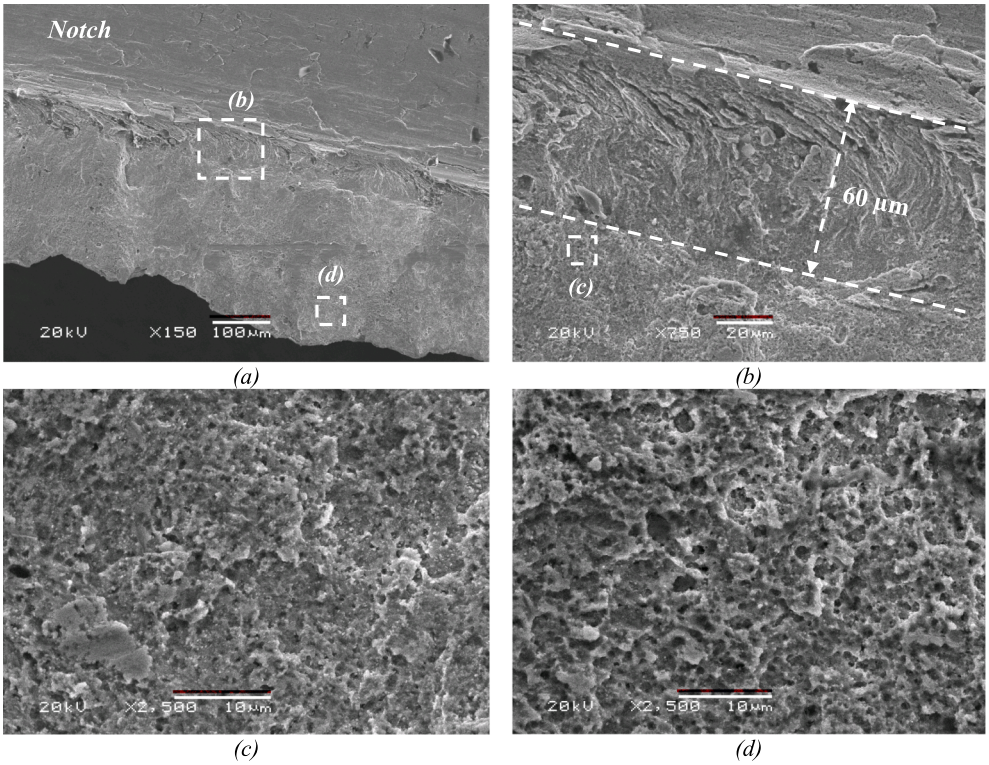

Fig. 15. Details of the fracture surface corresponding to the H-precharged specimen and tested at 52 MPa/h where EI P_b ~ 20 % and EI NMOD ~ 33 %. (a) General fracture surface. (b) MLD micromechanism. (c) CMD micromechanism and (d) Microvoid coalescence (final fracture in the bulk of the specimen).

the notched region. Nevertheless, a peripheral belt, of approximately 100 µm (Fig. 18a), characterized by CMD micromechanism was clearly observed (Fig. 18b). Coalescence of microvoids (MVC) was finally appreciated in the bulk of the specimen.

5. Conclusions

The present study has evaluated the hydraulic fracture behavior in the presence of internal hydrogen in a quenched and tempered steel (tempered martensite). By means of the cathodic hydrogen precharge (1.2 mA/cm^2 for 3 h at RT), ~1 ppm of hydrogen has been introduced within the steel microstructure (quenched & tempered steel). The hydrogen apparent diffusion coefficient has been estimated to be $7{\cdot}10^{-11}$ m^2/s. A trapping density in the range of $2{\cdot}10^{24}$ sites/m^3 was also found.

Hydrogen effect was notably appreciated as testing time increased until 2 h. The burst pressure is reduced around 28 % whilst the

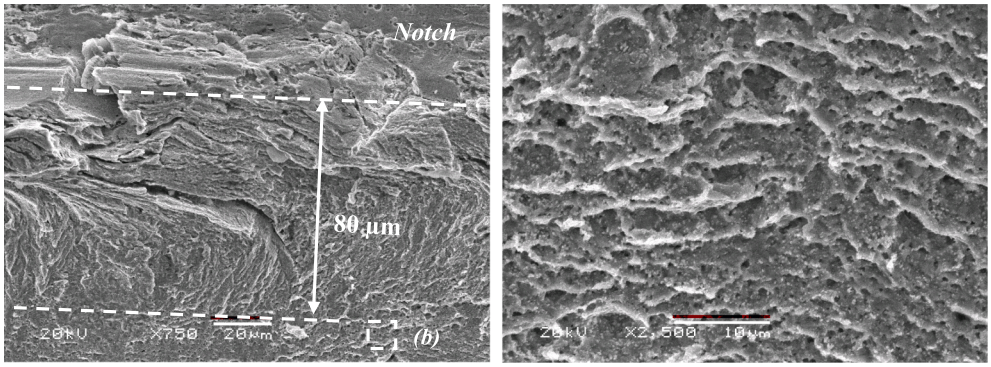

Fig. 16. Details of the fracture surface corresponding to the H-precharged specimen and tested at 35 MPa/h where EI P_b ~ 28 % and EI NMOD ~ 50 %. (a) MLD and secondary cracks. (b) quasi-cleavage with CMD micromechanism.

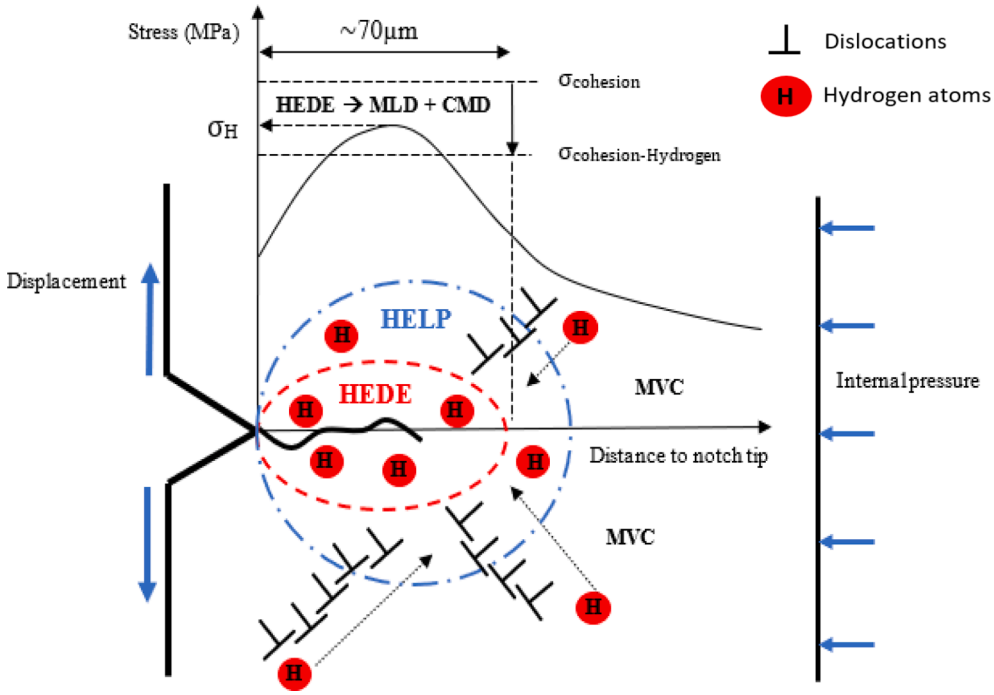

Fig. 17. HELP mediated HEDE mechanism in the notched region. Martensitic lath decohesion (MLD), carbides-matrix decohesion (CMD) and microvoids coalescence (MVC).

NMOD parameter decreased approximately 50 %. Accordingly, important changes on the fracture surfaces were observed. In absence of hydrogen, the fracture micromechanism was totally ductile. However, the fracture micromechanism changes from ductile to quasi-brittle in the presence of internal hydrogen, being this effect especially substantial in the specimens tested at 52 and 25 MPa/h, respectively, where MLD and CMD micromechanims based on HEDE mechanism were clearly appreciated.

Lastly, hydrogen precharged specimens gradually lose hydrogen during the hydraulic fracture tests, especially, after more than 2 h testing. Therefore, it is important to control the total duration of hydraulic fracture tests in order to appreciate the effect of internal hydrogen on the hydraulic fracture performance.

6. Data availability statement

The data that sustain the findings of this study are available from the corresponding author (lbperal@ubu.es), prior reasonable request.

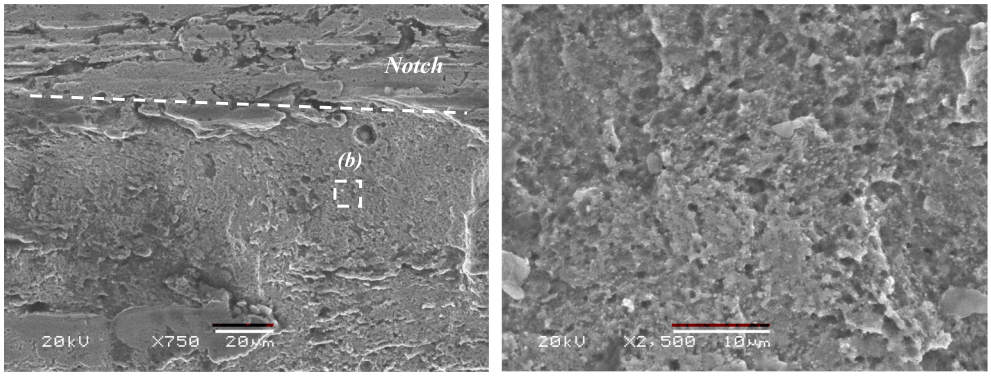

Fig. 18. Details of the fracture surface corresponding to the H-precharged specimen and tested at 25 MPa/h where EI $P_b \sim 13$ % and EI NMOD ~ 16 %. (a) Fracture surface near the notch region (with high hydrostatic stress) and (b) CMD micromechanism.

CRediT authorship contribution statement

L.B. Peral: Conceptualization, Data curation, Writing – original draft, Writing – review & editing, Visualization, Investigation, Formal analysis, Methodology. **A. Díaz:** Conceptualization, Writing – original draft, Writing – review & editing, Visualization, Investigation, Formal analysis, Methodology, Software. **V. Arniella:** Data curation, Investigation. **J. Belzunce:** Funding acquisition, Supervision, Resources, Project administration. **J. Alegre:** Funding acquisition, Validation, Supervision, Resources, Project administration. **I.I. Cuesta:** Conceptualization, Funding acquisition, Investigation, Validation, Methodology, Supervision, Resources, Project administration.

Declaration of Competing Interest

The authors declare that they have no known competing financial interests or personal relationships that could have appeared to influence the work reported in this paper.

Acknowledgments

The authors would like to thank the Spanish Government for the financial support received to perform the research projects RTI2018-096070-B-C33 and PID2021-124768OB-C21. L.B. Peral is grateful for his Margarita Salas Postdoctoral contract (Ref.: MU-21-UP2021-030) funded by the University of Oviedo through the Next Generation European Union.

References

[1] Ballantyne AP, Alden CB, Miller JB, Tans PP, White JWC. Increase in observed net carbon dioxide uptake by land and oceans during the past 50 years. Nature 2012;488:70–2. https://doi.org/10.1038/nature11299.
[2] Pillot S, Coudreuse L. Hydrogen-induced disbonding and embrittlement of steels used in petrochemical refining. Gaseous Hydrogen Embrittlement of Materials in Energy Technologies, Elsevier; 2012, p. 51–93. https://doi.org/10.1533/9780857093899.1.51.
[3] Macadre A, Artamonov M, Matsuoka S, Furtado J. Effects of hydrogen pressure and test frequency on fatigue crack growth properties of Ni–Cr–Mo steel candidate for a storage cylinder of a 70MPa hydrogen filling station. Engng Fract Mech 2011;78:3196–211. https://doi.org/10.1016/j.engfracmech.2011.09.007.
[4] Peral LB, Zafra A, Blasón S, Rodríguez C, Belzunce J. Effect of hydrogen on the fatigue crack growth rate of quenched and tempered CrMo and CrMoV steels. Int J Fatigue 2019;120:201–14. https://doi.org/10.1016/j.ijfatigue.2018.11.015.
[5] Álvarez G, Peral LB, Rodríguez C, García TE, Belzunce FJ. Hydrogen embrittlement of structural steels: Effect of the displacement rate on the fracture toughness of high-pressure hydrogen pre-charged samples. Int J Hydrogen Energy 2019;44:15634–43. https://doi.org/10.1016/j.ijhydene.2019.03.279.
[6] Shinko T, Halm D, Benoit G, Hénaff G. Controlling factors and mechanisms of fatigue crack growth influenced by high pressure of gaseous hydrogen in a commercially pure iron. Theor Appl Fract Mech 2021;112:102885. https://doi.org/10.1016/j.tafmec.2020.102885.
[7] Colombo C, Fumagalli G, Bolzoni F, Gobbi G, Vergani L. Fatigue behavior of hydrogen pre-charged low alloy Cr–Mo steel. Int J Fatigue 2016;83:2–9. https://doi.org/10.1016/j.ijfatigue.2015.06.002.
[8] Nagao A, Smith CD, Dadfarnia M, Sofronis P, Robertson IM. The role of hydrogen in hydrogen embrittlement fracture of lath martensitic steel. Acta Materialia 2012;60:5182–9. https://doi.org/10.1016/j.actamat.2012.06.040.
[9] Peral LB, Zafra A, Belzunce J, Rodríguez C. Effects of hydrogen on the fracture toughness of CrMo and CrMoV steels quenched and tempered at different temperatures. Int J Hydrogen Energy 2019;44:3953–65. https://doi.org/10.1016/j.ijhydene.2018.12.084.
[10] Momotani Y, Shibata A, Tsuji N. Hydrogen embrittlement behaviors at different deformation temperatures in as-quenched low-carbon martensitic steel. Int J Hydrogen Energy 2022;47:3131–40. https://doi.org/10.1016/j.ijhydene.2021.10.169.
[11] Cho L, Bradley PE, Lauria DS, Connolly MJ, Seo EJ, Findley KO, et al. Effects of hydrogen pressure and prior austenite grain size on the hydrogen embrittlement characteristics of a press-hardened martensitic steel. Int J Hydrogen Energy 2021;46(47):24425–39.
[12] Martiniano GA, Silveira Leal JE, Rosa GS, Bose Filho WW, Piza Paes MT, Franco SD. Effect of specific microstructures on hydrogen embrittlement susceptibility of a modified AISI 4130 steel. Int J Hydrogen Energy 2021;46:36539–56. https://doi.org/10.1016/j.ijhydene.2021.08.147.
[13] Li H, Venezuela J, Zhou Q, Shi Z, Yan M, Knibbe R, et al. Effect of shearing prestrain on the hydrogen embrittlement of 1180 MPa grade martensitic advanced high-strength steel. Corros Sci 2022;199:110170.

[14] Singh Raman RK, Rihan R, Ibrahim RN. Validation of a novel approach to determination of threshold for stress corrosion cracking (KISCC). Mater Sci Engng, A 2007;452–453:652–6. https://doi.org/10.1016/j.msea.2006.11.067.
[15] Raykar NR, Singh Raman RK, Maiti SK, Choudhary L. Investigation of hydrogen assisted cracking of a high strength steel using circumferentially notched tensile test. Mater Sci Engng, A 2012;547:86–92. https://doi.org/10.1016/j.msea.2012.03.086.
[16] Singh DK, Singh Raman RK, Maiti SK, Bhandakkar TK, Pal S. Investigation of role of alloy microstructure in hydrogen-assisted fracture of AISI 4340 steel using circumferentially notched cylindrical specimens. Mater Sci Engng, A 2017;698:191–7. https://doi.org/10.1016/j.msea.2017.05.056.
[17] Martin ML, Dadfarnia M, Nagao A, Wang S, Sofronis P. Enumeration of the hydrogen-enhanced localized plasticity mechanism for hydrogen embrittlement in structural materials. Acta Materialia 2019;165:734–50. https://doi.org/10.1016/j.actamat.2018.12.014.
[18] Djukic MB, Bakic GM, Sijacki Zeravcic V, Sedmak A, Rajicic B. The synergistic action and interplay of hydrogen embrittlement mechanisms in steels and iron: Localized plasticity and decohesion. Engng Fract Mech 2019;216:106528. https://doi.org/10.1016/j.engfracmech.2019.106528.
[19] Díaz A, Alegre JM, Cuesta II. A review on diffusion modelling in hydrogen related failures of metals. Engng Fail Anal 2016;66:577–95. https://doi.org/10.1016/j.engfailanal.2016.05.019.
[20] Peral LB, Amghouz Z, Colombo C, Fernández-Pariente I. Evaluation of hydrogen trapping and diffusion in two cold worked CrMo(V) steel grades by means of the electrochemical hydrogen permeation technique. Theor Appl Fract Mech 2020;110:102771. https://doi.org/10.1016/j.tafmec.2020.102771.
[21] Frappart S, Feaugas X, Creus J, Thebault F, Delattre L, Marchebois H. Study of the hydrogen diffusion and segregation into Fe–C–Mo martensitic HSLA steel using electrochemical permeation test. J Phys Chem Solids 2010;71:1467–79. https://doi.org/10.1016/j.jpcs.2010.07.017.
[22] Shi R, Chen L, Wang Z, Yang X-S, Qiao L, Pang X. Quantitative investigation on deep hydrogen trapping in tempered martensitic steel. J Alloy Compd 2021;854:157218. https://doi.org/10.1016/j.jallcom.2020.157218.
[23] Oudriss A, Fleurentin A, Courlit G, Conforto E, Berziou C, Rébéré C, et al. Consequence of the diffusive hydrogen contents on tensile properties of martensitic steel during the desorption at room temperature. Mater Sci Engng, A 2014;598:420–8.
[24] Peral LB, Fernández-Pariente I, Colombo C, Rodríguez C, Belzunce J. The Positive Role of Nanometric Molybdenum-Vanadium Carbides in Mitigating Hydrogen Embrittlement in Structural Steels. Materials 2021;14:7269. https://doi.org/10.3390/ma14237269.
[25] Peral LB, Zafra A, Fernández-Pariente I, Rodríguez C, Belzunce J. Effect of internal hydrogen on the tensile properties of different CrMo(V) steel grades: Influence of vanadium addition on hydrogen trapping and diffusion. Int J Hydrogen Energy 2020;45:22054–79. https://doi.org/10.1016/j.ijhydene.2020.05.228.
[26] Martínez-Pañeda E, Díaz A, Wright L, Turnbull A. Generalised boundary conditions for hydrogen transport at crack tips. Corros Sci 2020;173:108698. https://doi.org/10.1016/j.corsci.2020.108698.
[27] Díaz A, Alegre JM, Cuesta II. Numerical simulation of hydrogen embrittlement and local triaxiality effects in notched specimens. Theor Appl Fract Mech 2017;90:294–302. https://doi.org/10.1016/j.tafmec.2017.06.017.
[28] Li X, Zhang J, Akiyama E, Wang Y, Li Q. Microstructural and crystallographic study of hydrogen-assisted cracking in high strength PSB1080 steel. Int J Hydrogen Energy 2018;43:17898–911. https://doi.org/10.1016/j.ijhydene.2018.07.158.
[29] Yu H, Olsen JS, Alvaro A, Olden V, He J, Zhang Z. A uniform hydrogen degradation law for high strength steels. Engng Fract Mech 2016;157:56–71. https://doi.org/10.1016/j.engfracmech.2016.02.001.
[30] Zafra A, Álvarez G, Belzunce J, Rodríguez C. Influence of tempering time on the fracture toughness of hydrogen pre-charged 42CrMo4 steel. Theor Appl Fract Mech 2022;117:103197. https://doi.org/10.1016/j.tafmec.2021.103197.
[31] Zhang S, Xu D, Huang F, Gao W, Wan J, Liu J. Mitigation of hydrogen embrittlement in ultra-high strength lath martensitic steel via Ta microalloying. Mater Des 2021;210:110090. https://doi.org/10.1016/j.matdes.2021.110090.
[32] Kim H-J, Jeon S-H, Yang W-S, Yoo B-G, Chung Y-D, Ha H-Y, et al. Effects of titanium content on hydrogen embrittlement susceptibility of hot-stamped boron steels. J Alloy Compd 2018;735:2067–80.
[33] Zhang S, Huang Y, Sun B, Liao Q, Lu H, Jian B, et al. Effect of Nb on hydrogen-induced delayed fracture in high strength hot stamping steels. Mater Sci Engng, A 2015;626:136–43.
[34] Zafra A, Belzunce J, Rodríguez C, Fernández-Pariente I. Hydrogen embrittlement of the coarse grain heat affected zone of a quenched and tempered 42CrMo4 steel. Int J Hydrogen Energy 2020;45:16890–908. https://doi.org/10.1016/j.ijhydene.2020.04.097.
[35] Filho CJC, Mansur MB, Modenesi PJ, Gonzalez BM. The effect of hydrogen release at room temperature on the ductility of steel wire rods for pre-stressed concrete. Mater Sci Engng, A 2010;527:4947–52. https://doi.org/10.1016/j.msea.2010.04.042.
[36] Sofronis P, McMeeking RM. Numerical analysis of hydrogen transport near a blunting crack tip. J Mech Phys Solids 1989;37:317–50. https://doi.org/10.1016/0022-5096(89)90002-1.
[37] Dadfarnia M, Sofronis P, Neeraj T. Hydrogen interaction with multiple traps: Can it be used to mitigate embrittlement? Int J Hydrogen Energy 2011;36:10141–8. https://doi.org/10.1016/j.ijhydene.2011.05.027.
[38] Zafra A, Peral LB, Belzunce J. Hydrogen diffusion and trapping in A 42CrMo4 quenched and tempered steel: Influence of tempering temperature. Int J Hydrogen Energy 2020;45:31225–42. https://doi.org/10.1016/j.ijhydene.2020.08.134.
[39] Takeda Y, McMahon CJ. Strain controlled vs stress controlled hydrogen induced fracture in a quenched and tempered steel. Metall Trans A 1981;12:1255–66. https://doi.org/10.1007/BF02642339.